

Developing Ni single-atom sites in carbon nitride for efficient photocatalytic H₂O₂ production

Received: 28 April 2023

Accepted: 24 October 2023

Published online: 06 November 2023

Check for updates

Xu Zhang^{1,10}, Hui Su^{2,3,10}, Peixin Cui⁴, Yongyong Cao⁵, Zhenyuan Teng⁶, Qitao Zhang⁷, Yang Wang⁸, Yibo Feng¹, Ran Feng¹, Jixiang Hou¹, Xiyuan Zhou¹, Peijie Ma¹, Hanwen Hu¹, Kaiwen Wang¹, Cong Wang¹, Liyong Gan⁸, Yunxuan Zhao⁹, Qinghua Liu²✉, Tierui Zhang⁹✉ & Kun Zheng¹✉

Photocatalytic two-electron oxygen reduction to produce high-value hydrogen peroxide (H₂O₂) is gaining popularity as a promising avenue of research. However, structural evolution mechanisms of catalytically active sites in the entire photosynthetic H₂O₂ system remains unclear and seriously hinders the development of highly-active and stable H₂O₂ photocatalysts. Herein, we report a high-loading Ni single-atom photocatalyst for efficient H₂O₂ synthesis in pure water, achieving an apparent quantum yield of 10.9% at 420 nm and a solar-to-chemical conversion efficiency of 0.82%. Importantly, using in situ synchrotron X-ray absorption spectroscopy and Raman spectroscopy we directly observe that initial Ni-N₃ sites dynamically transform into high-valent O₁-Ni-N₂ sites after O₂ adsorption and further evolve to form a key *OOH intermediate before finally forming HOO-Ni-N₂. Theoretical calculations and experiments further reveal that the evolution of the active sites structure reduces the formation energy barrier of *OOH and suppresses the O=O bond dissociation, leading to improved H₂O₂ production activity and selectivity.

As one of the top 100 chemicals in the world, hydrogen peroxide (H₂O₂) is a high-value green oxidant and an emerging clean liquid fuel^{1,2}. Meanwhile, H₂O₂ is widely used in medical sterilization, printing, bleaching, waste water treatment and other fields, which is closely related to human life and social development^{3–6}. At present, the traditional anthraquinone method for large-scale industrial production of H₂O₂ has serious shortcomings such as high energy consumption,

intensive waste, and toxic by-products^{7,8}. Photocatalytic O₂ reduction to H₂O₂ by solar-driven semiconductor catalysts using H₂O and O₂ (2e⁻ ORR, O₂ + 2e⁻ + 2H⁺ → H₂O₂) is a green, economical, and promising H₂O₂ production strategy, which has been attracting extensive attention^{3,9–12}. Especially, photocatalytic efficient synthesis of H₂O₂ in pure water (without adding any sacrificial agent or buffer salt solution), which not only saves costs but also ensures the subsequent practical

¹Beijing Key Laboratory of Microstructure and Properties of Solids, Faculty of Materials and Manufacturing, Beijing University of Technology, Beijing 100124, China. ²National Synchrotron Radiation Laboratory, University of Science and Technology of China, Hefei 230029 Anhui, China. ³College of Chemistry and Chemical Engineering, Hunan Normal University, Changsha 410081 Hunan, China. ⁴Key Laboratory of Soil Environment and Pollution Remediation, Institute of Soil Science, Chinese Academy of Sciences, 210008 Nanjing, China. ⁵College of Biological, Chemical Science and Engineering, Jiaying University, Jiaying 314001 Zhejiang, China. ⁶School of Chemistry, Chemical Engineering and Biotechnology, Nanyang Technological University, Singapore 637459, Singapore. ⁷International Collaborative Laboratory of 2D Materials for Optoelectronics Science and Technology of Ministry of Education, Institute of Microscale Optoelectronics, Shenzhen University, Shenzhen 518060, China. ⁸College of Physics and Institute of Advanced Interdisciplinary Studies, Chongqing University, Chongqing 400044, China. ⁹Key Laboratory of Photochemical Conversion and Optoelectronic Materials, Technical Institute of Physics and Chemistry, Chinese Academy of Sciences, Beijing, China. ¹⁰These authors contributed equally: Xu Zhang, Hui Su. ✉e-mail: qhliu@ustc.edu.cn; tierui@mail.ipc.ac.cn; kunzheng@bjut.edu.cn

application of high-purity H_2O_2 (avoiding complicated and expensive distillation purification), is one of the goals pursued in this field^{4,9,10,13–17}. Among various photocatalysts, the low-cost graphitic carbon nitride ($\text{g-C}_3\text{N}_4$) has shown great potential for H_2O_2 production due to the certain light-responsive ability, suitable energy band structure, and metal-free structure suppression of H_2O_2 surface decomposition^{10,14,18–21}. However, the highest solar-to-chemical conversion (SCC) efficiency of the currently developed $\text{g-C}_3\text{N}_4$ -based photocatalysts for H_2O_2 production in pure water is still less than 0.65%^{10,13,14,22–24}, and the unsatisfactory catalytic activity restricts the industrial production and practical application of photocatalytic H_2O_2 synthesis. Therefore, further development of highly active photocatalysts for H_2O_2 production in pure water is of great significance and presents challenges.

The photocatalytic activity is considered to be the cumulative result of surface reactions between the active sites on the catalyst and the reactants^{25,26}. Several improved strategies (such as introducing surface defects^{14,27}, doping atoms^{18,28,29}, designing donor-acceptor units^{13,15,30}, forming heterojunctions^{11,22,31}, and developing metal/organic frameworks^{32–35}, etc.) have been developed to enhance photocatalytic H_2O_2 activity. However, due to the structural complexity caused by these strategies, identifying the dynamic structural evolution of active sites in photocatalytic surface reaction and elucidating the corresponding catalytic enhancement mechanism remains a great challenging and, as a result, is rarely reported. In pure water system, understanding how the active sites specifically participate in O_2 adsorption and activation during photoactivation at the atomic scale is a fundamental prerequisite for further enhancing the activity of 2e^- ORR, which is crucial for the rational development of high-performance 2e^- ORR photocatalysts. Excitingly, single-atom photocatalysts (SAPs) with well-defined single-atom active sites and high atomic utilization, serving as idealized catalytic models, provide opportunities for in-depth exploration of the active sites structure evolution and the reaction mechanism^{36–38}. Although SAPs have achieved some promising results in 2e^- ORR, it still faces the following key problems: (1) Most studies ignore the microscopic structural control of semiconductor substrates in SAPs, resulting in low single-atom loading that cannot provide abundant active sites, making the H_2O_2 generation activity in pure water unsatisfactory. (2) More urgently, the dynamic structural evolution of the active sites and corresponding catalytic enhancement mechanism in photocatalytic 2e^- ORR under practical reaction conditions remain unclear, severely limiting the further design and development of highly active photocatalysts for H_2O_2 synthesis in pure water.

Herein, we report a general method (by tuning the substrate microstructure and optimizing the loading process) for the synthesis of SAPs with high single-atom loading based on $\text{g-C}_3\text{N}_4$, and successfully synthesize a series of high-loading M-SAPs ($\text{M}=\text{Fe}, \text{Co}, \text{Ni}, \text{Cu}, \text{Zn}, \text{Sr}, \text{W}, \text{Pt}$) with porous ultrathin structures. Benefiting from the high-concentration single-atom sites exposed by this structure, the developed high-loading Ni single-atom photocatalyst ($\text{Ni}_{\text{SAPs}}\text{-PuCN}$) exhibits high activity and selectivity for H_2O_2 generation. Notably, in pure water, the apparent quantum yield (AQY) at 420 nm reaches 10.9% while achieving a high SCC efficiency of 0.82%, which is the most efficient $\text{g-C}_3\text{N}_4$ -based photocatalyst for H_2O_2 production reported so far. Pioneeringly, combining in situ synchrotron X-ray absorption spectroscopy, Raman spectroscopy, and theoretical calculation, we directly observed the transformation of initial Ni-N_3 sites into high-valent $\text{O}_1\text{-Ni-N}_2$ sites after O_2 adsorption during photoactivation. This process promotes the formation of the key intermediate $^*\text{OOH}$, which further transforms into HOO-Ni-N_2 . Crucially, the structure of the $\text{O}_1\text{-Ni-N}_2$ intermediate state ensures the end-on adsorption state of O_2 and suitable O_2 adsorption energy, leading to a fast transition from $\cdot\text{O}_2^-$ to $\cdot\text{OOH}$. Overall, this self-optimization of Ni active site evolution ($\text{Ni-N}_3 \rightarrow \text{O}_1\text{-Ni-N}_2 \rightarrow \text{HOO-Ni-N}_2$) greatly reduces the formation energy barrier

of the intermediate $^*\text{OOH}$ to accelerate H_2O_2 generation ($\text{O}_2 \rightarrow \cdot\text{O}_2^- \rightarrow \cdot\text{OOH} \rightarrow \text{H}_2\text{O}_2$), which is the core factor for the high activity and selectivity H_2O_2 production of $\text{Ni}_{\text{SAPs}}\text{-PuCN}$. Revealing the catalytic enhancement mechanism through the dynamic structural evolution of active sites provides insights for the development of highly active photocatalysts and a deeper understanding of photocatalysis.

Results and discussion

A general synthesis strategy for high-loading M-SAPs

Increasing the loading of single atoms to create more active sites is beneficial to improve the catalytic activity^{39,40}. A schematic diagram illustrating the synthesis of high-loading M-SAPs is presented in Fig. 1a, along with the presumed structural changes in the heptazine unit of the corresponding $\text{g-C}_3\text{N}_4$. Briefly, the synthesis of high-loading M-SAPs is primarily divided into two steps: regulating the microtopography and further optimizing the loading process (involving continuous ultrasonic treatment in wet-chemical precipitation). Firstly, the substrate

microtopography was adjusted by thermal stripping and ultrasonic exfoliation of the original bulk $\text{g-C}_3\text{N}_4$ (denoted as BCN), thereby preparing porous ultrathin $\text{g-C}_3\text{N}_4$ nanosheets (denoted as PuCN), which are beneficial for providing more sites for single-atom loading. Next, PuCN was further loaded with metal single atoms by wet-chemical precipitation under continuous ultrasonic conditions. The continuous ultrasonic treatment can not only promote the uniform dispersion of single atoms, but also further exfoliate $\text{g-C}_3\text{N}_4$ (destroy the van der Waals forces between carbon nitride layers) to provide abundant loading sites, and finally achieve a high-loading M-SAPs with a porous ultrathin structure (denoted as $\text{M}_{\text{SAPs}}\text{-PuCN}$, see “Methods” for details). Importantly, we further confirmed that this synthetic strategy is applicable for the preparation of a series of high-loading $\text{M}_{\text{SAPs}}\text{-PuCN}$ ($\text{M}=\text{Fe}, \text{Co}, \text{Ni}, \text{Cu}, \text{Zn}, \text{Sr}, \text{W}, \text{Pt}$). The aberration-corrected high-angle annular dark-field scanning transmission electron microscopy (HAADF-STEM) images in Fig. 1b–i reveal the uniform dispersion of high-density metal single atoms ($\text{Fe}, \text{Co}, \text{Ni}, \text{Cu}, \text{Zn}, \text{Sr}, \text{W}, \text{Pt}$) on $\text{g-C}_3\text{N}_4$, with no nanoclusters or particles observed. This observation is consistent with the X-ray diffraction (XRD, Supplementary Figs. 1, 2) results of all samples. Energy-dispersive X-ray spectroscopy (EDS, Supplementary Figs. 3–9) mapping further shows that C, N and M elements were uniformly distributed on $\text{g-C}_3\text{N}_4$. The content of metal loading in $\text{M}_{\text{SAPs}}\text{-PuCN}$ was all above 10 wt% by inductively coupled plasma mass spectrometry (ICP-MS, Supplementary Table 1).

Structural characterization of $\text{Ni}_{\text{SAPs}}\text{-PuCN}$

It was found that $\text{Ni}_{\text{SAPs}}\text{-PuCN}$ has the highest photocatalytic H_2O_2 generation activity among the prepared various $\text{M}_{\text{SAPs}}\text{-PuCN}$ (Supplementary Fig. 10); therefore, the structure of $\text{Ni}_{\text{SAPs}}\text{-PuCN}$ was further characterized in detail. The microstructure of the samples was investigated using HAADF-STEM, atomic force microscopy (AFM) and scanning electron microscopy (SEM). In Fig. 2a, BCN exhibited a thick-layered bulk structure, while the PuCN showed a distinct thin layer and porous structure (Fig. 2b). After the ultrasonic-wet chemical loading of Ni single atoms, more abundant pores and thinner undulating folds in $\text{Ni}_{\text{SAPs}}\text{-PuCN}$ can be clearly seen (Fig. 2c–d), which are also verified in AFM images (Supplementary Fig. 11). The decrease of the (002) peak intensity of $\text{Ni}_{\text{SAPs}}\text{-PuCN}$ in XRD (Supplementary Fig. 2) indicates the weakening of the interlayer stacking, which corresponds to the ultrathin structure. Meanwhile, SEM and TEM (Supplementary Fig. 12), N_2 physisorption measurements and pore size distribution (Supplementary Fig. 13 and Supplementary Table 2) together showed that the porous ultrathin structure of $\text{Ni}_{\text{SAPs}}\text{-PuCN}$ had a significantly increased specific surface area ($139.6 \text{ m}^2 \text{ g}^{-1}$, about 8.3 times of BCN) and abundant pore distribution. This adjusted structure would be very favorable for anchoring single atoms, as confirmed in the subsequent HAADF-STEM characterization (Fig. 2e and g). In Fig. 2e, numerous isolated

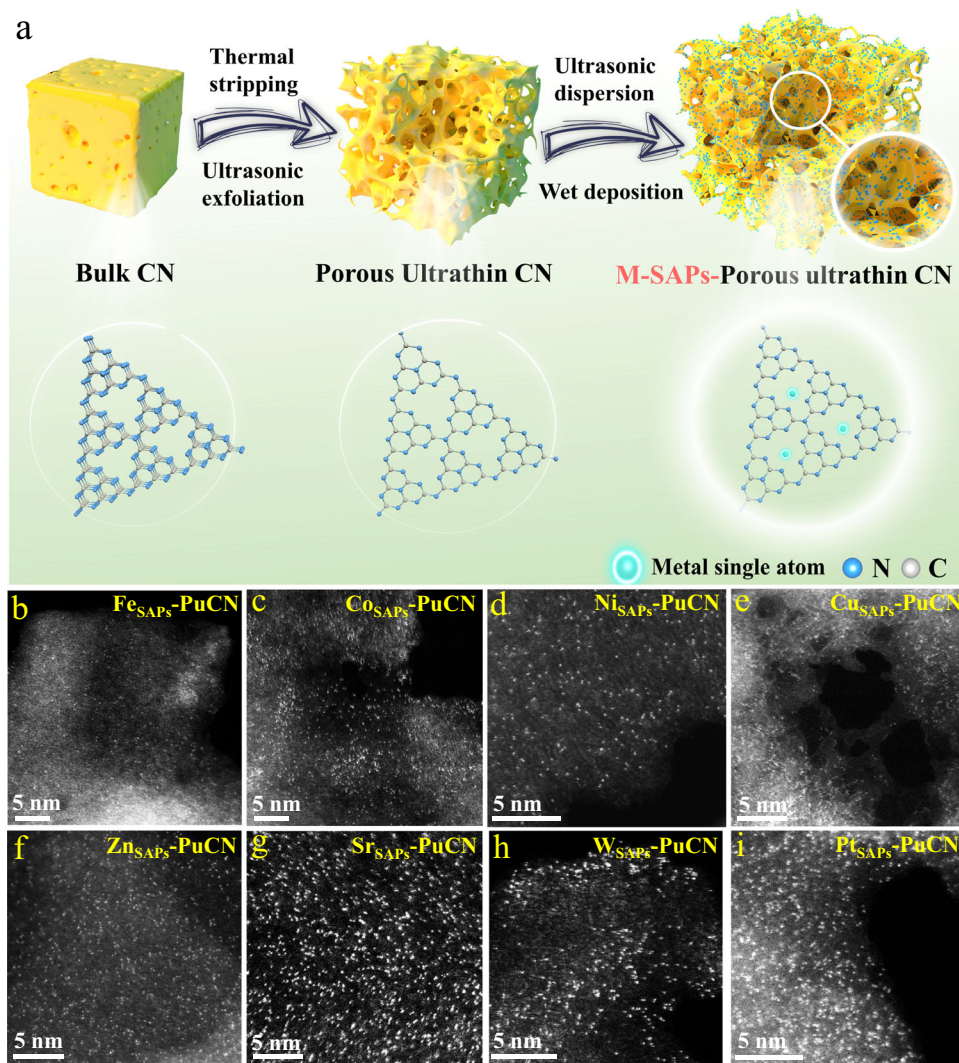


Fig. 1 | Synthesis and characterization of high-loading single-atom photocatalysts based on g-C₃N₄ (M_{SAPs}-PuCN). **a** Schematic diagram of the synthesis of high-loading M_{SAPs}-PuCN. **b–i** Aberration-corrected HAADF-STEM images of M_{SAPs}-PuCN (M = Fe, Co, Ni, Cu, Zn, Sr, W, Pt).

bright spots clearly differ from the g-C₃N₄ substrate contrast (See Supplementary Fig. 14a–c for more details), indicating that the high density of Ni single atoms was successfully dispersed on the Ni_{SAPs}-PuCN without any nanoparticles or clusters being found. The EDS mapping (Fig. 2f) showed that Ni, C and N elements were uniformly distributed on the ultrathin porous substrate. As shown in Fig. 2g, high-density Ni single atoms are anchored around the pores of Ni_{SAPs}-PuCN, which is favorable for the adsorption and activation of reaction gases in the shuttle pores. The Ni content in Ni_{SAPs}-PuCN was as high as 12.5 wt% measured by ICP-MS. In addition, the Fourier transform infrared spectroscopy (FTIR) and X-ray photoelectron spectroscopy (XPS) demonstrated that this synthesis method maintains the structure of g-C₃N₄ (Supplementary Fig. 15). Therefore, based on the above systematic characterizations, high-density Ni_{SAPs}-PuCN with porous ultrathin structure was successfully synthesized, and the schematic structure is shown in Fig. 2h.

Furthermore, the coordination structure of Ni in Ni_{SAPs}-PuCN was confirmed by X-ray absorption fine structure spectroscopy (XAFS). Figure 3a shows the Ni K-edge X-ray absorption near-edge structure (XANES) spectra of Ni_{SAPs}-PuCN and Ni foil, NiO, and NiPc as comparisons. The absorption edge position of Ni_{SAPs}-PuCN was located between Ni foil and NiO, suggesting that the valence state of Ni in Ni_{SAPs}-PuCN was between 0 and +2. The Fourier transform of the

extended X-ray absorption fine structure (FT-EXAFS) spectra of the samples is shown in Fig. 3b. The Ni_{SAPs}-PuCN exhibits a main peak around 1.69 Å (Fig. 3b), which is mainly attributed to the scattering interaction between Ni atoms and the first layer (Ni-N). However, no peak of Ni-Ni bond at about 2.17 Å was observed in Ni_{SAPs}-PuCN compared to Ni foil. This indicates that Ni species exists in the form of single atoms in Ni_{SAPs}-PuCN, validating the results of HAADF-STEM and XRD. Moreover, the wavelet transform (WT) in the Ni K-edge EXAFS further analyzes the coordination environment of Ni in Ni_{SAPs}-PuCN. Unlike Ni foil and NiO (Fig. 3f and Fig. 3g), the WT contour plot of Ni_{SAPs}-PuCN (Fig. 3e) shows that there is only one intensity maximum around 5.23 Å⁻¹ (attributed to Ni-N coordination), indicating Ni sites are atomically dispersed on Ni_{SAPs}-PuCN. The best-fit analysis results of EXAFS (Fig. 3d and Supplementary Table 3) show that each Ni atom in Ni_{SAPs}-PuCN is bonded with three N atoms as Ni-N₃ coordination, and the average Ni-N bond length is about 2.07 Å. The inset of Fig. 3c shows the Ni-N₃ coordination structure model in Ni_{SAPs}-PuCN, and the simulated XANES spectra based on this agree well with the experimental results (Fig. 3d), illustrating the rationality of the Ni-N₃ sites. Moreover, further theoretical calculations (Supplementary Fig. 16) also support the fitting results of Ni-N₃. In addition, thermodynamic and kinetic calculation results (Supplementary Fig. 14d–g) clearly demonstrate the rationality and stability of Ni single atoms on g-C₃N₄, consistent with

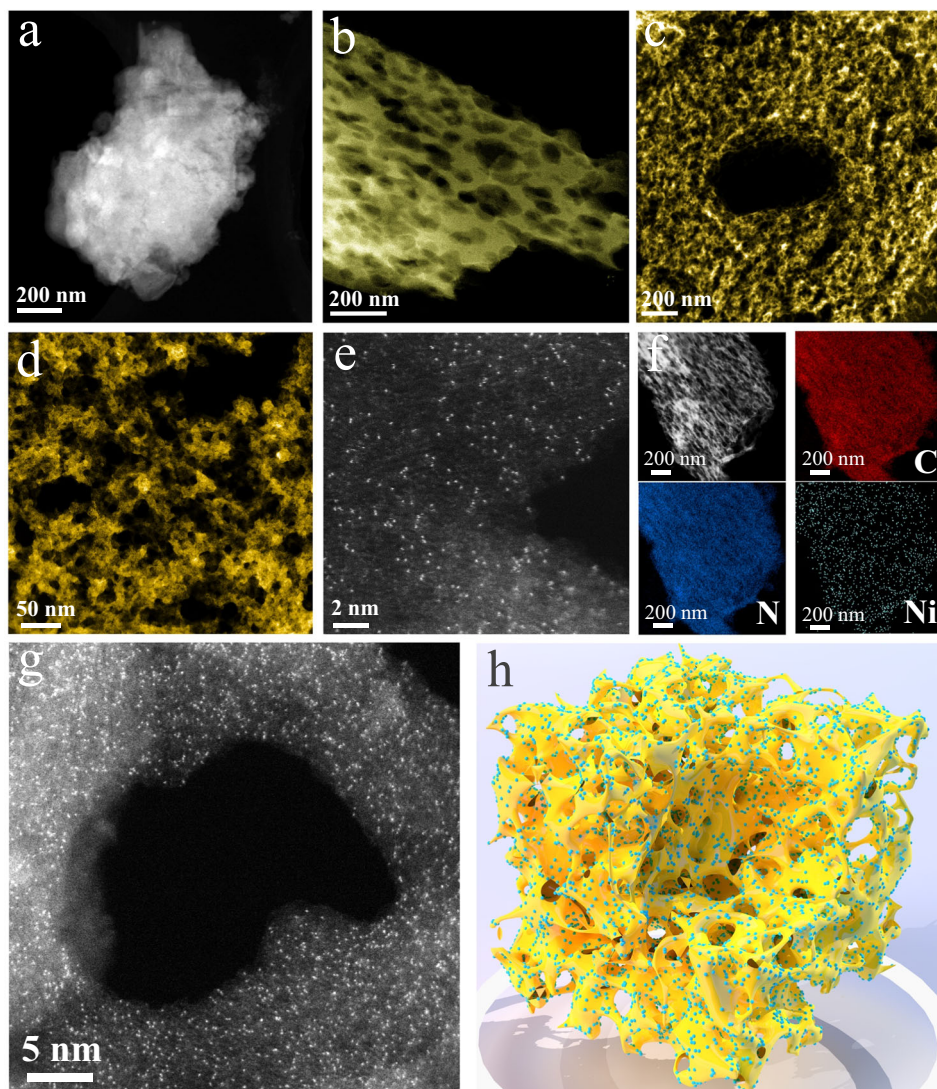


Fig. 2 | Structural characterization of Ni_{SAPs}-PuCN. **a–c** HAADF-STEM images of BCN, PuCN, and Ni_{SAPs}-PuCN (morphological structure). **d** Local magnification HAADF-STEM image of Ni_{SAPs}-PuCN. **e, g**, Aberration-corrected HAADF-STEM

images of Ni_{SAPs}-PuCN at different positions. **f** EDS mapping images of Ni_{SAPs}-PuCN. **h** Schematic structure of Ni_{SAPs}-PuCN.

experimental characterization results, in which Ni atoms exist as isolated single atoms rather than in the form of clusters.

Catalytic activity and selectivity of Ni_{SAPs}-PuCN for photocatalytic H₂O₂ production

The photocatalytic H₂O₂ generation performance of the samples was evaluated in O₂-saturated pure water (without any sacrificial agent or buffer salt solution; pH = 7) under visible light irradiation ($\lambda \geq 420$ nm). As shown in Fig. 4a, the H₂O₂ generation rate of PuCN ($41.1 \mu\text{mol L}^{-1} \text{h}^{-1}$) was slightly increased relative to BCN ($16.5 \mu\text{mol L}^{-1} \text{h}^{-1}$), which could be the porous ultrathin structure expanded the contact range of O₂. Notably, the Ni_{SAPs}-PuCN exhibited significantly enhanced H₂O₂ generation rate up to $342.2 \mu\text{mol L}^{-1} \text{h}^{-1}$ (Fig. 4a), which was 20.7 and 8.3 times of BCN and PuCN, respectively (Fig. 4b). This indicates that the Ni single atoms are the core of the enhanced H₂O₂ production activity. Meanwhile, the effect of Ni single atoms loading content and Ni nanoparticles on the H₂O₂ activity was further sorted out (Supplementary Figs. 17, 18). Furthermore, the H₂O₂ generation activity of Ni_{SAPs}-PuCN can be improved to $640.1 \mu\text{mol L}^{-1} \text{h}^{-1}$ under AM 1.5G irradiation (Fig. 4b). The variable comparison and radical trapping experiments.

(Supplementary Fig. 19) confirm that H₂O₂ is indeed generated by the 2e⁻ ORR pathway. The oxidation reaction of photogenerated holes was confirmed by photocatalytic O₂ production test (Supplementary Fig. 20), which is consistent with previous reports¹⁰. The final yield of photocatalytic H₂O₂ production depends on the formation and decomposition rates of H₂O₂, and the experiment (Supplementary Fig. 21) suggested that the decomposition rate of H₂O₂ on the samples is relatively slow. A systematic performance comparison of Ni_{SAPs}-PuCN with recently reported g-C₃N₄-based materials and other types of materials for photocatalytic H₂O₂ production in pure water is presented in Supplementary Table 4. The comparison of corresponding normalized H₂O₂ yields ($\mu\text{mol g}^{-1} \text{h}^{-1}$) in Supplementary Fig. 22 demonstrates the efficient H₂O₂ generation activity of Ni_{SAPs}-PuCN.

To further evaluate the light utilization efficiency of Ni_{SAPs}-PuCN in pure water, the AQY was measured under monochromatic light irradiation (Fig. 4c and Supplementary Table 5). The AQY of Ni_{SAPs}-PuCN at 420 nm reaches 10.9%, surpassing most of reported g-C₃N₄-based photocatalysts and currently developed materials (Supplementary Fig. 23 for AQY comparison and Supplementary Table 4). Moreover, in Fig. 4f, the SCC efficiency of Ni_{SAPs}-PuCN can reach 1.17% in the first hour and finally stabilized at 0.82% in 3 h, which is the

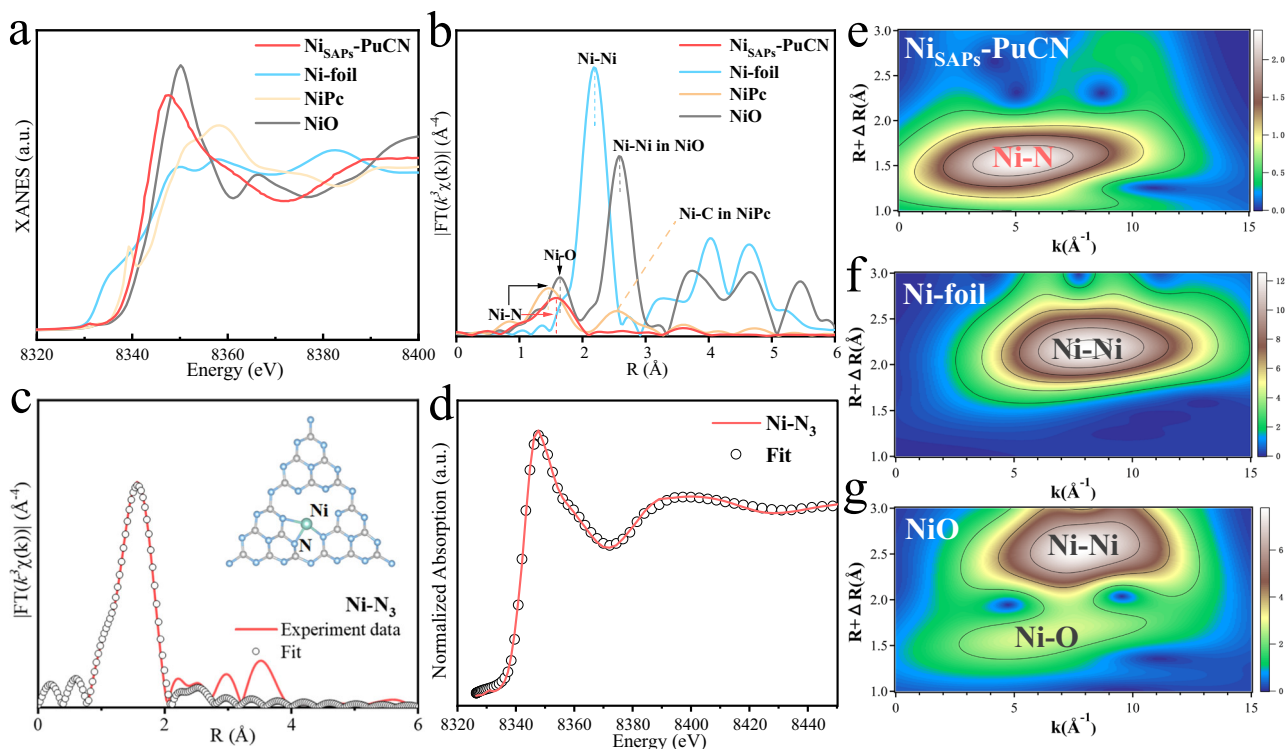


Fig. 3 | Ni single atoms coordination structure characterization in Ni_{SAPs}-PuCN. **a** Ni *K*-edge XANES spectra of Ni_{SAPs}-PuCN, Ni-foil, NiO, and NiPc. **b** Fourier transformation of the EXAFS spectra. **c** First-shell (Ni-N) fitting of Fourier

transformations of EXAFS spectra for Ni_{SAPs}-PuCN. **d** Simulated XANES spectra based on Ni-N₃ model for DFT calculations. **e–g** Wavelet transform EXAFS spectra of Ni_{SAPs}-PuCN, Ni-foil, and NiO, respectively.

highest value reported so far for g-C₃N₄-based photocatalysts in pure water (Fig. 4g for SCC efficiency comparison and Supplementary Table 4). Simultaneously, in Fig. 4g, when compared with other types of photocatalysts currently developed, the SCC efficiency of Ni_{SAPs}-PuCN still demonstrates advantages and approaches the highest SCC efficiency values (1.0%–1.2%) reported for powder photocatalyst^{15,30}. Overall, according to the standard H₂O₂ yield, AQY and SCC efficiency as the evaluation indicators of photocatalytic activity, Ni_{SAPs}-PuCN has excellent H₂O₂ generation activity in pure water. Meanwhile, Ni_{SAPs}-PuCN exhibited excellent performance cyclability (Supplementary Fig. 24) and structural stability (Supplementary Fig. 25a–f). The thermodynamic stability of the Ni_{SAPs}-PuCN model was also confirmed by molecular dynamics (MD) calculations (Supplementary Fig. 25g).

The high ORR selectivity is the guarantee of high activity^{2,4}. The effect of Ni single atoms on O₂ selective electron transfer was investigated by electrochemical measurements on rotating ring-disk electrode (RRDE), where the disk current was derived from the reduction reaction of O₂, while the ring current was derived from the oxidation reaction of the produced H₂O₂. The selectivity of H₂O₂ generation on BCN and Ni_{SAPs}-PuCN was monitored in O₂-saturated 0.1M KOH electrolyte. In Fig. 4d (bottom), the reduction disk currents of PCN and Ni_{SAPs}-PuCN gradually increased as the potential decreased from 0.8 V (vs. RHE). In Fig. 4d (top), the ring current of Ni_{SAPs}-PuCN was significantly higher than that of BCN, indicating that Ni_{SAPs}-PuCN produced more H₂O₂. As shown in Fig. 4e, the average number of transferred electrons (*n*) and H₂O₂ selectivity were calculated in the potential range of 0–0.6 V (vs. RHE). Under the same conditions, the number of transferred electrons of Ni_{SAPs}-PuCN is closer to 2 and the selectivity of H₂O₂ is higher than that of BCN. The number of electrons transferred on BCN was 2.77, and the H₂O₂ selectivity was only 61.4% at 0.5 V (vs. RHE). But at the same potential, the number of electrons transferred on Ni_{SAPs}-PuCN is 2.14, achieving 92.4% H₂O₂ selectivity. Combined with the RRDE and photocatalytic H₂O₂ performance tests, these fully demonstrate that Ni

single-atom sites greatly improve the 2e⁻ selectivity of O₂ and efficiently promote H₂O₂ generation.

Electronic Structure and carrier separation properties of Ni_{SAPs}-PuCN

The electronic structure of photocatalysts largely determines the carrier separation characteristics and further affects the surface reaction efficiency^{19,26,41,42}. In the UV-Vis diffuse reflectance spectroscopy (DRS) of the samples (Supplementary Fig. 26a), the introduction of Ni single atoms expands the absorption of visible light and adjusts the band structure. The introduction of Ni single atoms effectively promotes carrier separation and transport, as confirmed by a series of spectroscopic measurements (Supplementary Fig. 27). Next, femto-second transient absorption spectroscopy (fs-TAS) was used to further investigate the kinetic behaviors of the photogenerated carriers. The results indicate that Ni_{SAPs}-PuCN has a shorter lifetime than BCN (See Supplementary Fig. 28 for more details), which could be attributed to the deep trapping sites induced by Ni single atoms and has been demonstrated to facilitate the 2e⁻ ORR process¹⁰. Bader charge analysis (Supplementary Fig. 29) indicates that the chemical valence of Ni single-atom in Ni_{SAPs}-PuCN is positive, which is in line with the results of Ni 2p XPS (Supplementary Fig. 15d) and XANES (Fig. 3a). The total density of states (TDOS) of BCN exhibits a typical semiconducting nature (Supplementary Fig. 30a), where the valence band (VB) are mainly composed of N 2p orbitals, while the conduction band (CB) is mainly composed of C 2p and N 2p orbitals^{43,44}. As for Ni_{SAPs}-PuCN, the introduction of Ni atoms creates impurity levels and narrows the band gap (Supplementary Fig. 30b), which agrees well with the experimental results (Supplementary Fig. 26b). Combined with the projected density of states (PDOS) of Ni (Supplementary Fig. 31), the Ni 3d orbitals contribute to both CB and VB, implying that Ni single atoms greatly optimize the electronic structure. Further, in the charge density difference of Ni_{SAPs}-PuCN (Supplementary Fig. 32), there are remarkably

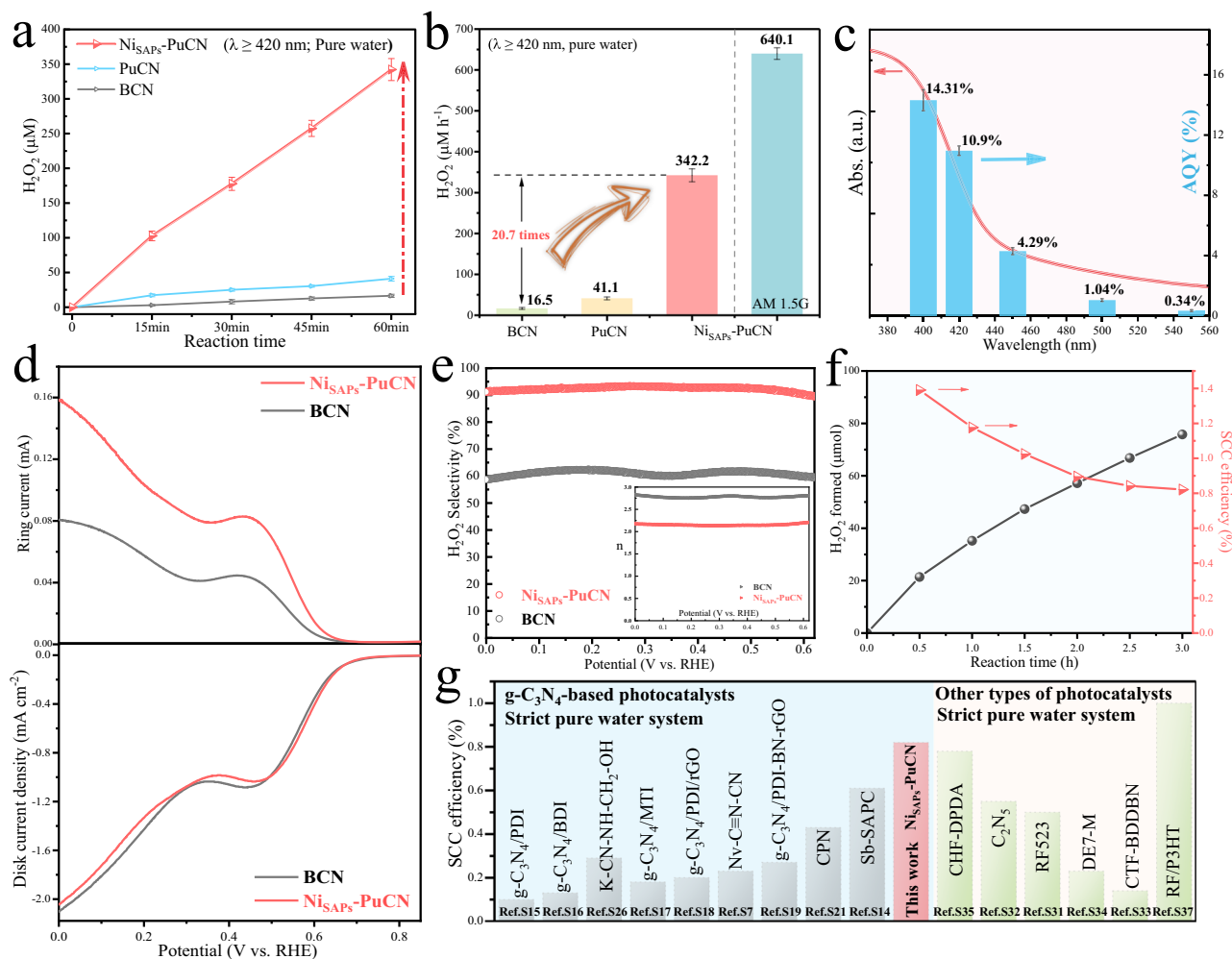


Fig. 4 | Photocatalytic H_2O_2 production activity and selectivity of $\text{Ni}_{\text{SAPs}}\text{-PuCN}$.

a The time course of H_2O_2 production measured in pure water under visible light irradiation ($\lambda \geq 420$ nm, 60 mW cm^{-2} ; 30 mg catalyst in 30 ml pure water, 1 g L^{-1} catalyst; 25°C). Error bars are the standard deviations of three replicate measurements. **b** Performance comparison of all samples in pure water under visible light conditions and H_2O_2 generation performance of $\text{Ni}_{\text{SAPs}}\text{-PuCN}$ under AM 1.5 G illumination (60 mW cm^{-2}). **c** The wavelength-dependent AQY for photocatalytic H_2O_2 production in pure water by $\text{Ni}_{\text{SAPs}}\text{-PuCN}$ (50 mg catalyst in 50 ml pure water, 1 g L^{-1}

catalyst, 25°C). **d** DRDE polarization curves over BCN and $\text{Ni}_{\text{SAPs}}\text{-PuCN}$ in O_2 -saturated 0.1 M KOH at 1600 rpm with ring current (upper part) and disk current (bottom part). **e** H_2O_2 selectivity as a function of the applied potential. The inset shows the calculated average number of transferred electrons (n). **f** The amount of H_2O_2 generated by $\text{Ni}_{\text{SAPs}}\text{-PuCN}$ under AM 1.5 G simulated sunlight irradiation (100 mW cm^{-2}) and the corresponding SCC efficiency (500 mg in 100 ml pure water, 25°C). **g** Summarized SCC efficiencies of recently reported photocatalysts ($\text{g-C}_3\text{N}_4$ -based and other types of photocatalysts) for H_2O_2 production in pure water.

charge redistribution between Ni single-atom and N atoms, which would help to facilitate the separation and transport of photo-generated carriers. The optimized carrier separation and transport properties of $\text{Ni}_{\text{SAPs}}\text{-PuCN}$ will facilitate subsequent efficient surface reactions.

In situ XAFS analysis of Ni-N₃ site evolution during photoactivation

To gain deep insight into the structural evolution of Ni sites and catalytic enhancement mechanism, in situ XAFS measurements were performed to monitor the details of O_2 adsorption and activation on Ni single atoms at the atomic scale. Figure 5a–b shows the normalized Ni K-edge XANES spectra and the corresponding FT-EXAFS spectra. As shown in Fig. 5a, in the Ar-saturated aqueous solution, the Ni single atoms in $\text{Ni}_{\text{SAPs}}\text{-PuCN}$ were still Ni-N₃ coordinated (Supplementary Fig. 33 and Table 6), indicating that the aqueous solution does not affect the Ni coordination structure. However, the white line intensity of the Ni K-edge XANES spectra was clearly enhanced in O_2 -saturated aqueous solution compared to the Ar-saturated aqueous solution (enlarged view of Fig. 5a). This indicates an increase in Ni oxidation

state, possibly due to the delocalization of unpaired electrons in Ni 3d orbitals and the spontaneous charge transfer from Ni to the O 2p orbitals of O_2 , which promotes the formation of superoxide radicals ($\cdot\text{O}_2^-$). Next, EPR experiments and theoretical calculations can provide evidence for our analysis. On the one hand, the $\cdot\text{O}_2^-$, as a key free radical for photocatalytic 2e^- ORR, is formed from the electron obtained by the activated O_2 ($\text{O}_2 + \text{e}^- \rightarrow \cdot\text{O}_2^-$)^{10,14}. The EPR trapping experiments further confirmed the presence of $\cdot\text{O}_2^-$. As shown in Fig. 5f, compared with the dark condition, $\text{Ni}_{\text{SAPs}}\text{-PuCN}$ under the light condition had a stronger $\cdot\text{O}_2^-$ signal, corresponding to Ni losing electrons (resulting in an increased oxidation state) and transferring electrons to O_2 to generate $\cdot\text{O}_2^-$. On the other hand, based on theoretical calculations, the optimized structure and charge difference density of $\text{Ni}_{\text{SAPs}}\text{-PuCN}$ after adsorption of O_2 are shown in Fig. 5d, which can intuitively reflect the charge transfer from Ni sites to the end-on adsorbed O_2 ($\text{O}_1\text{-Ni-N}_2$). Detailed theoretical calculations illustrated the plausibility of $\text{O}_1\text{-Ni-N}_2$ after O_2 adsorption (Supplementary Fig. 34). Furthermore, this charge transport mechanism was confirmed again based on Bader charge analysis, where the adsorbed O_2 molecules gain electrons (0.48|e|) from $\text{Ni}_{\text{SAPs}}\text{-PuCN}$ (Fig. 5d). Based on the above results, to further

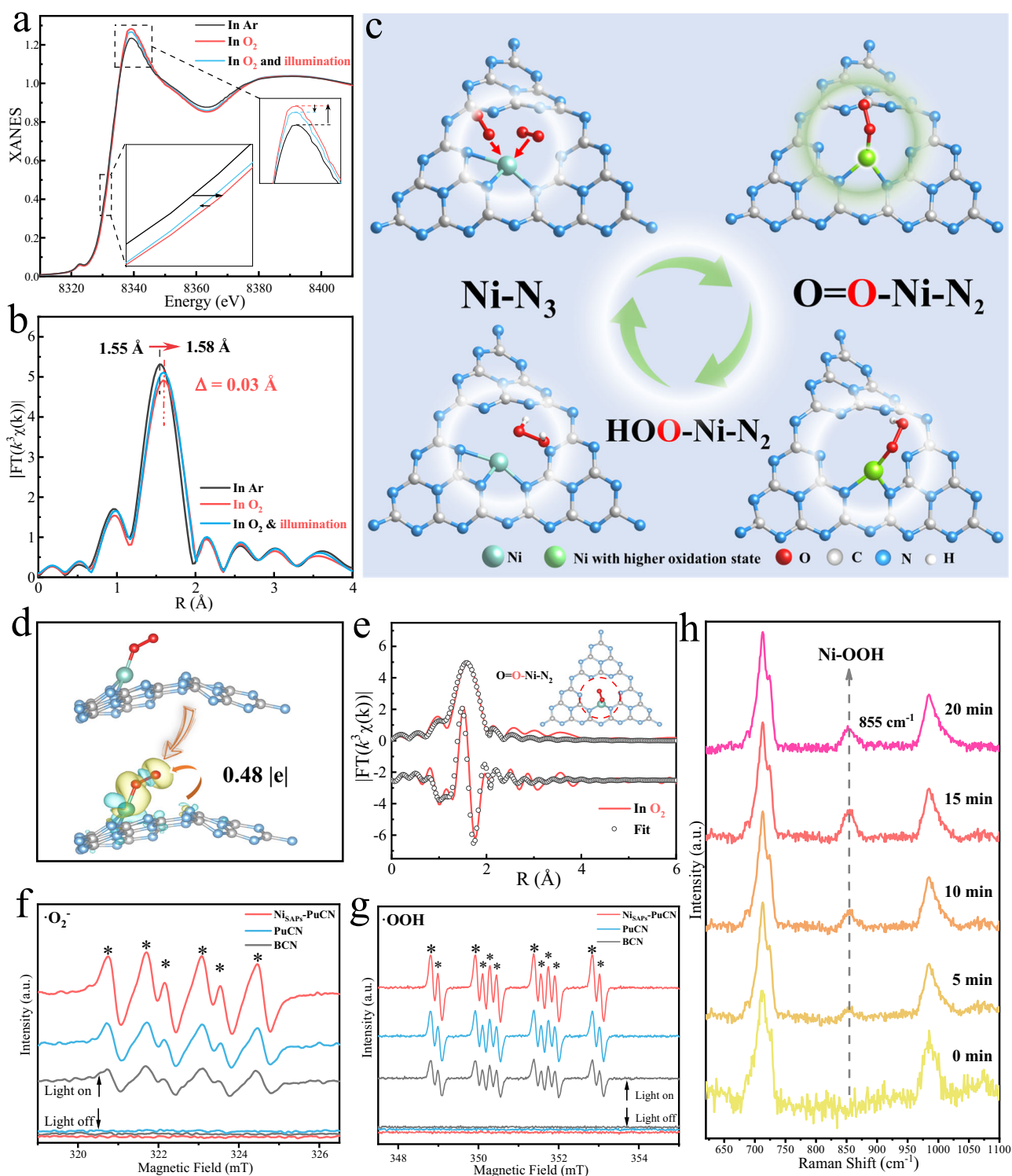


Fig. 5 | In situ structural evolution of Ni sites in photocatalytic 2e⁻ ORR. **a** Ni *K*-edge XANES spectra of NiSAPs-PuCN during photocatalytic 2e⁻ ORR in Ar or O₂ saturated aqueous solution at room temperature. The inset is the enlarged Ni *K*-edge XANES spectra. **b** FT-EXAFS spectra of NiSAPs-PuCN under in situ operation. **c** Schematic diagram of Ni sites structure evolution of NiSAPs-PuCN in the photocatalytic 2e⁻ ORR. **d** Optimized structures and charge difference density of

adsorbed O₂ molecule on NiSAPs-PuCN (The isosurface value is 0.0016 eV Å⁻³, electron accumulation and consumption are indicated in yellow and blue, respectively). **e** First-shell fitting of FT-EXAFS spectra for NiSAPs-PuCN in O₂ saturated aqueous solution. **f, g** EPR signals of ·O₂⁻ and ·OOH of the samples in the presence of DMPO. **h** Raman spectra of NiSAPs-PuCN recorded during the photoreaction in O₂-saturated aqueous solution.

elucidate the local coordination structure evolution of the Ni active sites in O₂, the Ni *K*-edge EXAFS fitting results (Fig. 5e and Supplementary Table 6) in O₂-saturated solution revealed additional Ni-O coordination (bond length about 2.10 Å), fitted as O₁-Ni-N₂

coordination (schematic inset of Fig. 5e). The above results comprehensively demonstrate that the active sites of NiSAPs-PuCN evolved from the initial Ni-N₃ to O₁-Ni-N₂ at the O₂ adsorption and activation stages.

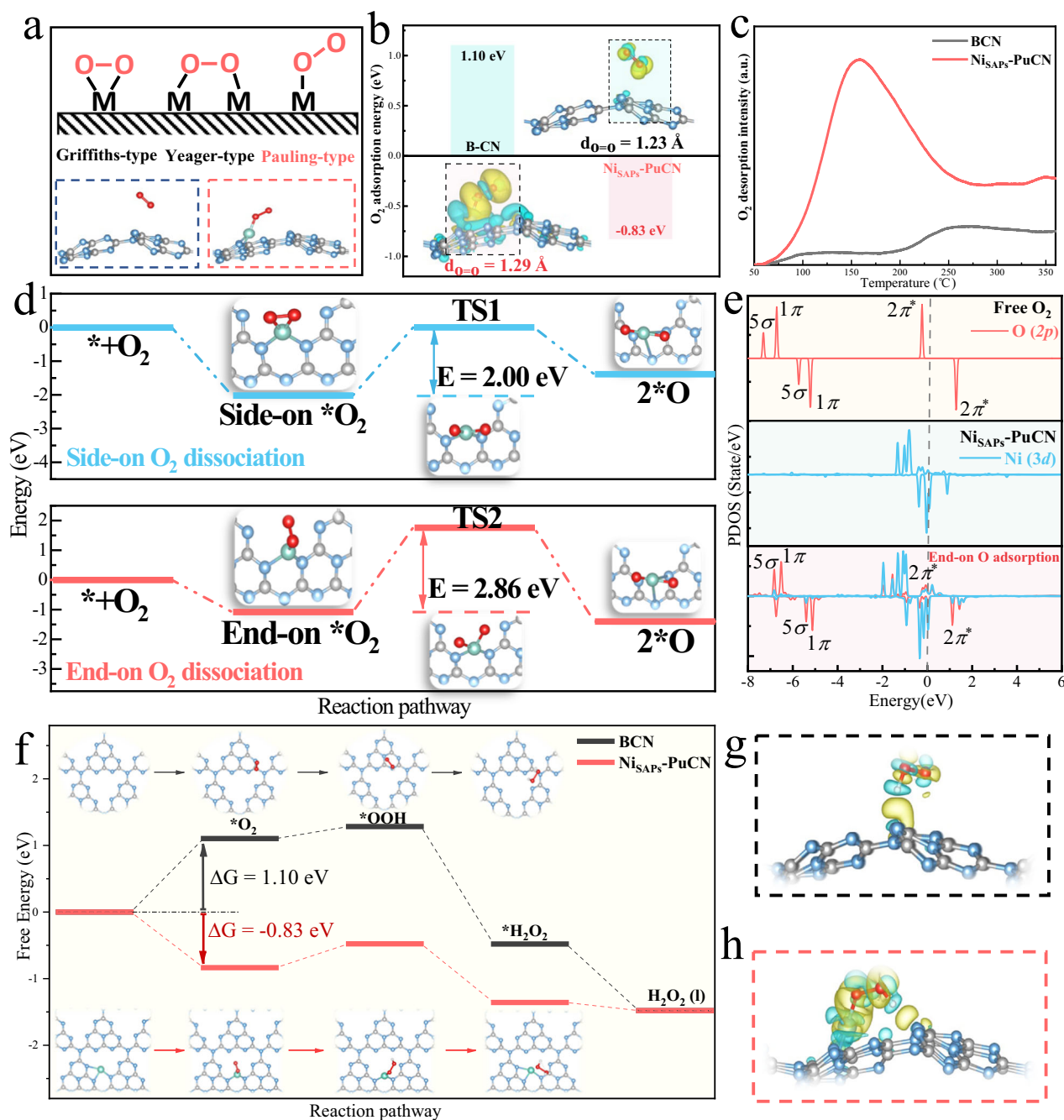


Fig. 6 | Catalytic enhancement mechanism of Ni sites evolution in Ni_{SAPs}-PuCN. **a** Schematic diagram of O₂ adsorption structure for metal sites (upper part), and optimized structures of adsorbed O₂ molecule on BCN and Ni_{SAPs}-PuCN (bottom part). **b** Comparison of O₂ adsorption energy and charge difference density on BCN and Ni_{SAPs}-PuCN. **c** Temperature programmed O₂ desorption (TPD-O₂) profiles of BCN and Ni_{SAPs}-PuCN. **d** O₂ dissociation energies and profile corresponding to Ni_{SAPs}-PuCN side-on (upper part) and end-on O₂ (bottom part) adsorption

configurations. **e** The PDOS plots for free O₂, Ni_{SAPs}-PuCN and Ni_{SAPs}-PuCN after end-on O₂ adsorption. **f** Free energy profiles for photocatalytic H₂O₂ evolution reactions over BCN and Ni_{SAPs}-PuCN. Optimized models and charge difference density after BCN (**g**) and Ni_{SAPs}-PuCN (**h**) generate *OOH (The isosurface value is 0.0016 eV Å⁻³. Electron accumulation and consumption are indicated in yellow and blue, respectively).

Next, as shown in Fig. 5a, when light sources are introduced to initiate the photocatalytic 2e⁻ ORR, the Ni *K*-edge shifts to the lower energy direction (between the O₂-saturated aqueous solution and the Ar-saturated aqueous solution), corresponding to a decrease in the oxidation state. This suggests that the 2e⁻ ORR reaction is further driven (Ni(*) + O₂ + 2e⁻ + 2H⁺ → Ni(*) + H₂O₂; O₂ → ·O₂⁻ → ·OOH → H₂O₂). Nonetheless, it is difficult to accurately capture the key intermediate *OOH on the Ni site using in situ XAFS, so the Raman spectroscopy (Fig. 5h) was used to further identify the reaction details. In Fig. 5h,

Ni_{SAPs}-PuCN gradually exhibits a new absorption band at 855 cm⁻¹ in O₂ aqueous solution with illumination time, which can be attributed to the O=O stretching mode in Ni-OOH^{10,45,46}. Moreover, theoretical calculation (Supplementary Fig. 35) further reveal that the *OOH on the Ni sites is in an end-on adsorption configuration (HOO-Ni-N₂, Fig. 5c and Fig. 6h). Simultaneously, the ·OOH radicals were also detected through EPR test^{30,47}. In Fig. 5g, compared with BCN and PuCN, Ni_{SAPs}-PuCN had a stronger ·OOH signal under the same conditions, implying that Ni single atoms can effectively promote the ·OOH generation.

Throughout the in situ XAFS, the FT-EXAFS spectra (Fig. 5b) show that the main peak shifts (-0.03 \AA) to longer lengths, implying the expansion of the Ni-N bonds during the reaction. Thus, combined with the above comprehensive analysis, we elucidated the structural evolution mechanism of Ni active sites on Ni_{SAPs}-PuCN in photocatalytic 2e⁻ ORR, and the corresponding schematic diagram is shown in Fig. 5c. In photocatalytic 2e⁻ ORR, after O₂ adsorption and activation, the Ni-N₃ sites are transformed into O₁-Ni-N₂, which further promotes the formation of the key *OOH intermediate with end-on adsorption configuration (HOO-Ni-N₂), thereby accelerating the generation of H₂O₂.

In-depth exploration of Ni site structure evolution and catalytic enhancement mechanism

To further understand the relationship between structural evolution of Ni active sites and high H₂O₂ activity, we systematically investigated the surface reaction mechanism of 2e⁻ ORR by combining theoretical calculations and experiments. The first step of the 2e⁻ ORR surface reaction is O₂ adsorption and activation. The O₂ adsorption configuration and the O₂ adsorption energy on the catalyst are particularly critical for the subsequent reactions^{48,49}. The adsorption configuration of O₂ on the catalyst is categorized into three basic types (Fig. 6a, upper): Yeager type (side-on), Griffith type (side-on), and Pauling type (end-on)^{48,50}. The end-on O₂ adsorption configuration, which tends to maintain the O=O bond, can inhibit the 4e⁻ ORR ($\text{O}_2 + 4\text{e}^- + 4\text{H}^+ \rightarrow 2\text{H}_2\text{O}$) and promote the highly selective 2e⁻ ORR^{7,48,49,51}. Based on this, we first performed first-principles calculations to investigate the O₂ adsorption and activation properties in this system. As shown in the calculation results in Fig. 6a (bottom), in comparison to BCN, O₂ was adsorbed by Ni single atoms on Ni_{SAPs}-PuCN in an end-on configuration (O₁-Ni-N₂), which is consistent with the fitted data from in situ XAFS (Fig. 5e). Simultaneously, the O₂ adsorption Gibbs free energy on Ni_{SAPs}-PuCN (-0.83 eV , Fig. 6b) was much lower than that of BCN (1.10 eV , Fig. 6b), indicating that Ni single atoms can efficiently adsorb O₂. The charge difference density after O₂ adsorption on the two samples (inset of Fig. 6b) was further calculated and analyzed. Compared to BCN (the bond length of adsorbed O₂ on BCN is 1.23 \AA), the adsorbed O₂ on Ni_{SAPs}-PuCN has a longer O=O bond length (1.29 \AA) and a larger charge transfer, indicating that the O₁-Ni-N₂ intermediate structure promotes the O₂ adsorption and activation. Furthermore, temperature-programmed desorption of O₂ (TPD-O₂, Fig. 6c) suggested that Ni_{SAPs}-PuCN has remarkable stronger O₂ adsorption capacity than BCN, which fully confirms our calculation results.

In addition, maintaining the O=O bond of O₂ and avoiding the dissociation of O₂ are important prerequisites for H₂O₂ generation in 2e⁻ ORR^{4,52}. Different O₂ adsorption configurations affect the extent of O₂ activation and the subsequent reactions, and these effects were investigated through theoretical calculations. As shown in Fig. 6d, the O₂ dissociation barriers for side-on (O₂-Ni-N₂) and end-on O₂ adsorption configurations (O₁-Ni-N₂) on Ni_{SAPs}-PuCN are 2.00 eV and 2.86 eV , respectively. This indicates that the side-on adsorbed O₂-Ni-N₂ is more inclined to dissociate O₂, while the end-on adsorbed O₁-Ni-N₂ intermediate structure inhibits the dissociation of O₂ and favors the H₂O₂ generation, further emphasizing the importance of O₁-Ni-N₂ in the structural evolution. The PDOS was further used to elucidate the charge transfer between the end-on adsorbed O₂ molecule and Ni_{SAPs}-PuCN. As shown in Fig. 6e, when free O₂ with a spin triplet ground state is adsorbed onto Ni_{SAPs}-PuCN, the *2p* orbitals of O exhibit noticeable hybridization with the Ni *3d* orbitals of Ni_{SAPs}-PuCN. The O₂ molecule donates the *p*-electron to the empty *3d* orbital of the Ni atom, and then the *3d* electron from the Ni atom is donated back to the *2π** orbital of O₂. As a result, the original empty *2π** orbitals in the spin-down channel of free O₂ are partially occupied, leading to the elongation of the O=O bond length. Based on the above analysis, the improved O₂ adsorption and activation properties of Ni active sites provide strong support for

the formation of O₁-Ni-N₂ sites in in situ XAFS. Moreover, the critical intermediate state with the O₁-Ni-N₂ structure ensures suitable O₂ adsorption energy and adsorption configuration, inhibits O₂ dissociation, and improves the selectivity, thus guaranteeing the subsequent efficient H₂O₂ generation.

Based on the above results, the free energy changes of the photocatalytic 2e⁻ ORR on the BCN and Ni_{SAPs}-PuCN were further calculated. In Fig. 6f, the introduction of Ni active sites greatly facilitates the O₂ adsorption compared to BCN (reduced from 1.10 eV to -0.83 eV , and the theoretical calculation of BCN for O₂ adsorption is in Supplementary Fig. 36). The formation and hydrogenation of the core intermediate *OOH are also the key to 2e⁻ ORR^{10,14}. The enhanced O₂ adsorption capacity of Ni_{SAPs}-PuCN further facilitates *OOH formation, thus evidently promoting the conversion of *OOH to H₂O₂. Moreover, Fig. 6g–h shows the charge density difference between the two structures and the resulting *OOH. Contrast to BCN, the charge redistribution between *OOH and Ni_{SAPs}-PuCN is more remarkable, reflecting that Ni sites effectively promote the generation of key intermediate *OOH, which is also in line with the EPR test (Fig. 5g). Combined with the ·O₂⁻ and ·OOH radical tests of EPR (Fig. 5f–g), the highly active Ni_{SAPs}-PuCN has the strongest ·O₂⁻ and ·OOH signals in contrast, indicating that the evolution of the Ni site structure is accompanied by a rapid transformation mechanism from ·O₂⁻ to ·OOH, which strongly supports the above calculations. More importantly, theoretical simulations also confirm that the structural evolution of Ni sites (structure diagram in Fig. 6f) during this process is consistent with in situ experiments: from Ni-N₃ to O₁-Ni-N₂ to HOO-Ni-N₂, corresponding to the reaction mechanism from O₂ to ·O₂⁻ to ·OOH to H₂O₂. This dynamic structural evolution mechanism of Ni single atoms represents the self-optimization of active sites in 2e⁻ ORR surface reaction, which is the core factor for Ni_{SAPs}-PuCN with high activity and high selectivity for H₂O₂.

In summary, we present a general synthesis strategy for high-loading M_{SAPs}-PuCN (M = Fe, Co, Ni, Cu, Zn, Sr, W, Pt) with porous ultrathin structure. This approach can be applied to various catalytic reactions and energy conversion fields. The well-designed high-loading Ni_{SAPs}-PuCN exhibits excellent photocatalytic H₂O₂ performance, with Ni single atoms optimizing the electronic structure and providing numerous highly active reaction sites. Importantly, through in situ XAFS and theoretical calculations, we reveal the structural evolution of Ni single-atom active sites (Ni-N₃ → O₁-Ni-N₂ → HOO-Ni-N₂) in surface reactions, closely related to the high catalytic activity. The O₁-Ni-N₂ intermediate state structure ensures the proper O₂ adsorption configuration and energy, not only suppressing O₂ dissociation and enhancing the selectivity, but also promoting intermediate conversion to H₂O₂. This dynamic self-tuning of the coordination structural evolution significantly lowers the formation energy barrier of *OOH, which is a pivotal factor contributing to the high activity and selectivity of Ni_{SAPs}-PuCN. Elucidating the mechanism of structural evolution closely associated with high catalytic activity paves the way for the design of highly efficient photocatalysts and a deeper comprehension of photocatalysis.

Methods

Synthesis of BCN

10 g of urea was placed in a covered alumina crucible and heated to $550 \text{ }^\circ\text{C}$ at a rate of $5 \text{ }^\circ\text{C min}^{-1}$ in a muffle furnace for 2 h. After the crucible was cooled to room temperature, the product was collected and ground into powder, washed several times with deionized water, and dried under vacuum at $80 \text{ }^\circ\text{C}$ for 12 h (the obtained BCN was about 300 mg).

Synthesis of PuCN

The PuCN was obtained by thermal stripping and ultrasonic stripping of BCN. Similar to the synthesis of BCN, the holding time at $550 \text{ }^\circ\text{C}$ in the

muffle furnace was extended to 4 h. After cooling, 50 mg of the powder was ultrasonically stripped in 100 ml of pure water for 8 h and collected by centrifugation. The product was drop-coated evenly in glassware and dried overnight in vacuum (the obtained PuCN was about 45 mg).

Synthesis of Ni_{SAPs}-PuCN and various M_{SAPs}-PuCN

Put 50 mg of PuCN in 40 ml of pure water and add 10 ml of ethanol, first sonicate for 2 h to evenly disperse the sample. Then, under continuous ultrasonic and stirring, a certain amount of NiCl₂·6H₂O solution (45 mg of NiCl₂·6H₂O in 30 ml of solvent, 1.5 mg ml⁻¹; water to ethanol in the solvent is 1:1) was slowly added dropwise, and ultrasonically treated for 3 h to ensure full contact between metal ions and PuCN (continuous sonication is beneficial to promote uniform dispersion and high loading of single atoms, see Supplementary Fig. 37 for more details). The volume of Ni solution added (5 ml, 10 ml or 15 ml, etc.) is controlled to adjust the metal loading. Then the mixed solution was heated in an oil bath at 60 °C for 4 h with vigorous stirring. The product was collected by centrifugation and dried overnight at 80 °C in a vacuum oven. The powder was fully ground and heated to 350 °C in an Ar atmosphere at 2 °C min⁻¹ in a tube furnace and kept for 2 h, and finally cooled to room temperature. The collected powders were washed multiple times with 2% (v/v) HCl to remove nanoparticles or clusters, then washed at least 3 times with pure water and dried overnight in a vacuum oven at 80 °C to obtain Ni_{SAPs}-PuCN (about 40 mg). The maximum Ni single-atom loading in Ni_{SAPs}-PuCN is 12.5 wt %, and more details are shown in Supplementary Fig. 17 and Supplementary Table 1. The synthesis method of M_{SAPs}-PuCN is the same as that of Ni_{SAPs}-PuCN. Different metal salt solutions, such as FeCl₃·6H₂O, CoCl₂·6H₂O, CuCl₂, ZnCl₂, SrCl₂, Na₂WO₄·2H₂O and H₂PtCl₆, were used to prepare M_{SAPs}-PuCN (M = Fe, Co, Cu, Zn, Sr, W, Pt).

Photocatalytic H₂O₂ production reaction

30 mg of photocatalyst was placed in 30 ml of pure water (pH = 7), and ultrasonically treated for 30 min until the catalyst powder was completely dispersed. The solution was continuously filled with O₂ for 1 h in the dark to saturate the O₂. The reaction solution was irradiated with a 420 nm cut-off film ($\lambda \geq 420$ nm) under a 300 W Xe lamp (PLS-SXE 300D/DUV, PerfectLight) and started the photoreaction test under magnetic stirring. The flow rate of the O₂ was 50 ml min⁻¹ and the reaction temperature was controlled at 25 °C by circulating water. The average light intensity was 60 mW cm⁻². Every 15 min, 2 ml of the reaction solution was taken out, and the photocatalyst was removed by centrifugal filtration. The H₂O₂ content generated by the reaction was detected by iodometric method^{14,28}. Briefly, 0.5 ml of 0.4 mol L⁻¹ potassium iodide (KI) solution and 0.5 ml of 0.1 mol L⁻¹ potassium hydrogen phthalate (C₈H₅KO₄) solution was added to 1 ml obtained solution and kept for 30 min. The content of H₂O₂ was determined by absorbance at 350 nm with a UV-Vis spectrophotometer (The standard curve for H₂O₂ was shown in Supplementary Fig. 38). The effect of different catalyst concentrations on the photocatalytic H₂O₂ activity was also illustrated (Supplementary Fig. 39). More details of the process can be found in our previous paper¹⁴. The photocatalytic O₂ generation reaction was tested by connecting the reactor to a glass-enclosed gas system (Labsolar-6A, PerfectLight). Disperse 30 mg of the catalyst in 30 ml of pure water, and add AgNO₃ (20 mM) as an electron acceptor and 30 mg of La₂O₃ to stabilize the pH of the reaction system. N₂ was passed through the reactor for 30 min to remove residual gas. The generated O₂ was detected under visible light irradiation ($\lambda \geq 420$ nm) of a 300 W Xe lamp and by an online gas chromatograph (5 Å molecular sieve column, Ar carrier).

Determination of AQY efficiency

The AQY efficiency of Ni_{SAPs}-PuCN was tested under pure water (50 mg catalyst in 50 ml solution, pH = 7, 25 °C). AQY tests were performed using a 300 W Xe lamp (PLS-FX300HU, PerfectLight) with different

bandpass filters at 400, 420, 450, 500 and 550 nm (FWHM = 15 nm). The average light intensity was measured by an optical power meter (Thorlabs) and the irradiated area was controlled at 1.69 cm². AQY is calculated by the following Eq. (1):

$$\text{AQY} = \frac{2 \times \text{H}_2\text{O}_2 \text{ formed (mol)}}{\text{the number of incident photons (mol)}} \times 100\% \quad (1)$$

Measurement of SCC efficiency

The SCC efficiency was evaluated using a 300 W Xe lamp (PLS-FX300HU, PerfectLight) with an AM 1.5 G filter as a simulated sun light source. 500 mg of the catalyst was dispersed in 100 ml of pure water (pH = 7, 25 °C) with sufficient O₂ for photoreaction. The spot irradiation area is set to 1 cm², and the light intensity is strictly set to 100 mW cm⁻² (1 sun) by the optical power meter (Thorlabs). The SCC efficiency is calculated by the following Eq. (2):

$$\text{SCC} = \frac{[\Delta G_{\text{H}_2\text{O}_2}] \times [N_{\text{H}_2\text{O}_2}]}{I \times S \times T} \times 100\% \quad (2)$$

where $\Delta G_{\text{H}_2\text{O}_2}$ is the Gibbs free energy (117 KJ mol⁻¹) of forming H₂O₂, $N_{\text{H}_2\text{O}_2}$ is the amount of H₂O₂ produced, I is the light intensity of simulated sunlight (100 mW cm⁻²), S is the illuminated area (1 cm²), and T is the illuminated time (s).

Electrochemical measurement of O₂ reduction reaction (ORR)

The number of transferred electrons (n) and H₂O₂ selectivity of the samples in ORR were measured using a rotating ring disk electrode (RRDE). The electrochemical measurement adopts a three-electrode system, in which Pt/C is the counter electrode, RRDE is the working electrode, and Ag/AgCl is the reference electrode. The electrolyte is O₂ saturated 0.1 M KOH solution. The speed of RRDE was used at 1600 rpm and the potential range was set to 0–1.0 V vs. RHE. The catalyst ink on the RRDE working electrode is prepared as follows. After uniform grinding of 4 mg catalyst, it was ultrasonically dispersed in 400 μ L pure water, 600 μ L isopropanol and 10 μ L Nafion solution for 1 h. Next, 10 μ L of ink was dropped on the RRDE electrode and dried at room temperature. The number of transferred electrons is calculated according to the following Eq. (3):

$$n = \frac{4I_d}{I_d + I_r/N} \quad (3)$$

The H₂O₂ selectivity is calculated according to the following Eq. (4):

$$\text{H}_2\text{O}_2(\%) = 2 \times \frac{I_r/N}{I_d + I_r/N} \times 100\% \quad (4)$$

where I_r is the ring current, I_d is the disc current, and N is the collection efficiency (0.37).

Characterization

TEM, HAADF-STEM and EDS were collected on a spherical aberration-corrected transmission electron microscope FEI Titan Themis with an accelerating voltage of 300 KV. The surface morphology of the samples was characterized by SEM (Thermo Fisher Scientific Quattro S). The X-ray diffraction (XRD) patterns of the samples were collected on an X-ray diffractometer (Bruker D8) with Cu K α radiation at 40 kV and 40 mA. The Fourier transform infrared (FTIR) spectra were obtained on Bruker V70 spectrometer. The single-atom content in M_{SAPs}-PuCN was determined by inductively coupled plasma mass spectrometry (ICP-MS) on a PerkinElmer NexION 300X (samples were dissolved in aqua regia). X-ray photoelectron spectroscopy (XPS) measurements were acquired on an ESCALAB 250Xi instrument (Thermo Fisher Scientific) using Al K α radiation, and the calibration peak was C 1s at 284.8 eV. UV-Vis diffuse reflectance spectroscopy (DRS) of the samples

was collected on Shimadzu UV-3600 instrument with BaSO₄ as reference. Photoluminescence (PL) spectra were measured on a fluorescence spectrometer (Hitachi F-7000) with an excitation wavelength of 325 nm. Time-resolved photoluminescence (TRPL) spectra were collected on an Edinburgh FLS1000 fluorescence spectrometer with excitation at 375 nm. Raman spectra were acquired on a high-resolution confocal Raman spectrometer (RENISHAW inVia) with an excitation laser of 785 nm. The EPR signal generated by the samples in the 5,5-dimethyl-1-pyrroline N-oxide solution (DMPO) was captured using an A300-10/12 spectrometer. The N₂ adsorption-desorption isotherm and pore size distribution of the samples were measured at 77 K using a micrometrics Max-II system. Detection of temperature programmed O₂ desorption (TPD-O₂) of samples using a temperature-programmed chemisorption instrument (AutoChem1 II 2920). The electrochemical impedance spectroscopy (EIS) was measured on the electrochemical workstation (CHI600A) with a standard three-electrode system, in which the catalyst-coated ITO was the working electrode, the Pt wire was the counter electrode and the saturated calomel electrode was the reference electrode.

In situ XAFS measurement

The in situ XAFS measurements of Ni K-edge were carried out at the 1W1B station in the Beijing Synchrotron Radiation Facility (BSRF), China. The storage ring of BSRF was operated at 2.5 GeV with a maximum current of 250 mA. The beam from the bending magnet was monochromatized utilizing a Si (111) double-crystal monochromator and further detuning of 30% to remove higher harmonics. The photochemical in situ XAFS tests were performed by a home-made cell in a pure water solution. The XAFS spectra were collected through fluorescence mode. The Ni_{SAPs}-PuCN catalyst on 3D substrate was cut into 1 × 2 cm² pieces and then sealed in a cell by Kapton film. In order to obtain information on the evolution of active sites during photochemical reactions, a series of representative working conditions were applied to the samples, including Ar-saturated solution (In Ar), O₂ saturated solution (In O₂) and light conditions (visible light irradiation in O₂ saturated solution). A 300 W Xe lamp (PLS-SXE 300D/DUV, PerfectLight) with a 420 nm cut-off film (λ ≥ 420 nm) was utilized as the light source for the photocatalytic reaction. During the collection of XAFS measurements, the position of the absorption edge (E₀) was calibrated using a standard sample of Ni, and all XAFS data were collected during one period of beam time.

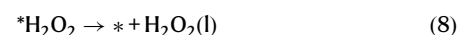
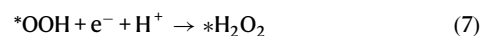
XAFS data analysis

The acquired EXAFS data were processed according to the standard procedures using the ATHENA module implemented in the IFEFFIT software packages. Subsequently, k³-weighted χ(k) data in the k-space ranging from 2.6–11.8 Å⁻¹ were Fourier transformed to real space using a Hanning window (dk = 1.0 Å⁻¹) to separate the EXAFS contributions from different coordination shells. The best background removal was at the R_{bkg} = 1.0 Å, and the low-frequency noise was removed fully. As for the Ni_{SAPs}-PuCN under saturated Ar solution, the curve fitting was done on the k³-weighted EXAFS function χ(k) data in the k-range of 2.6–11.8 Å⁻¹ and in the R-range of 1.0–2.2 Å. The number of independent points for these samples are N_{ipt} = 2ΔkΔR/π = 2 × (11.8 – 2.6) × (2.2 – 1.0)/π = 7. However, the first coordination peak of Ni_{SAPs}-PuCN under O₂ saturated solution conditions showed similar intensity and higher R shift compared with Ar-saturated solution, which was ascribed to the fracture of Ni-N bond and addition of Ni-O coordination. Therefore, the two subshells of Ni-N and Ni-O coordination were considered for the curve fitting of Ni_{SAPs}-PuCN under O₂ saturated solution. During curve fittings, each of the Debye-Waller factors (σ²), coordination numbers (N), interatomic distances (R), and energy shift (ΔE₀) was treated as adjustable parameters.

Computational methods

All density functional theory calculations were performed using the Perdew-Burke-Ernzerhof formulation within the generalized gradient approximation. These calculations were conducted with the Vienna Ab Initio Package^{53,54}. The projected augmented wave potential was chosen to describe the ion nucleus⁵⁵. The valence electrons were considered, using a plane wave basis set with a kinetic energy cutoff of 500 eV. Electron energies are considered self-consistent when the energy change is less than 10⁻⁵ eV. The geometry optimization was considered converged when the force change was smaller than 0.02 eV/Å. Grimme's DFT-D3 method is used to account for dispersion interactions⁵⁶.

The lattice constants of corrugated 2 × 2 g-C₃N₄ monolayer in a vacuum with a depth of 20 Å was optimized, when using a 2 × 2 × 1 k-point grid for Brillouin zone sampling, to be a = 13.674 Å. This model comprises of 24 C and 32 N atoms. This model and metal single-atom-doped ones were used for adsorption. The adsorption energy (E_{ads}) of adsorbate A was defined as: E_{ads} = E_{A/surf} – E_{surf} – E_{A(g)}, where E_{A/surf} represents the energy of the adsorbate A adsorbed on the surface, E_{surf} and E_{A(g)} is the energy of isolated A molecule in a cubic periodic box with a side length of 20 Å and a 1 × 1 × 1 Monkhorst-Pack k-point grid for Brillouin zone sampling, respectively. The free energy of gas-phase molecules or surface adsorbates is calculated from the equation G = E + ZPE – TS, where E is the total energy, ZPE is the zero-point energy, T is the temperature in Kelvin (298.15 K is set here), and S is the entropy. The overall reaction pathway for the calculated 2e⁻ ORR includes: (1) O₂ adsorption on the active site (*) in catalysts (Eq. 5); (2) the adsorbed O₂ captures an e⁻ and combines with H⁺ to form *OOH (Eq. 6); (3) *OOH continues the electron-coupled proton transfer reaction to form H₂O₂ (Eq. 7); (4) desorption and diffusion of H₂O₂ (Eq. 8).



Data availability

The data that support the findings of this study are available within the article and the Supplementary Information. The source data are available from the corresponding authors upon request.

References

- Perry, S. C. et al. Electrochemical synthesis of hydrogen peroxide from water and oxygen. *Nat. Rev. Chem.* **3**, 442–458 (2019).
- Xia, C., Kim, J. Y. & Wang, H. Recommended practice to report selectivity in electrochemical synthesis of H₂O₂. *Nat. Catal.* **3**, 605–607 (2020).
- Hou, H., Zeng, X. & Zhang, X. Production of hydrogen peroxide by photocatalytic processes. *Angew. Chem. Int. Ed. Engl.* **59**, 17356–17376 (2020).
- Tang, J. et al. Selective hydrogen peroxide conversion tailored by surface, interface, and device engineering. *Joule* **5**, 1432–1461 (2021).
- Xu, J. et al. Organic wastewater treatment by a single-atom catalyst and electrolytically produced H₂O₂. *Nat. Sustain.* **4**, 233–241 (2021).
- Xia, C., Xia, Y., Zhu, P., Fan, L., Wang, H. J. S. Direct electrosynthesis of pure aqueous H₂O₂ solutions up to 20% by weight using a solid electrolyte. **366**, 226–231 (2019).

- Gao, J. et al. Enabling direct H₂O₂ production in acidic media through rational design of transition metal single atom catalyst. *Chem.* **6**, 658–674 (2020).
- Yang, S. et al. Toward the decentralized electrochemical production of H₂O₂: a focus on the catalysis. *ACS Catal.* **8**, 4064–4081 (2018).
- Yu, W. et al. Photocatalytic hydrogen peroxide evolution: what is the most effective strategy? *Nano Energy* **104**, 107906 (2022).
- Teng, Z. et al. Atomically dispersed antimony on carbon nitride for the artificial photosynthesis of hydrogen peroxide. *Nat. Catal.* **4**, 374–384 (2021).
- Wu, Q. et al. A metal-free photocatalyst for highly efficient hydrogen peroxide photoproduction in real seawater. *Nat. Commun.* **12**, 483 (2021).
- Li, K. et al. Highly efficient photocatalytic H₂O₂ production in microdroplets: accelerated charges separation and transfer at interface. *Energy Environ. Sci.* **16**, 1135–1145 (2023).
- Shiraishi, Y. et al. Resorcinol-formaldehyde resins as metal-free semiconductor photocatalysts for solar-to-hydrogen peroxide energy conversion. *Nat. Mater.* **18**, 985–993 (2019).
- Zhang, X. et al. Unraveling the dual defect sites in graphite carbon nitride for ultra-high photocatalytic H₂O₂ evolution. *Energy Environ. Sci.* **15**, 830–842 (2022).
- Shiraishi, Y., Matsumoto, M., Ichikawa, S., Tanaka, S. & Hirai, T. Polythiophene-doped resorcinol-formaldehyde resin photocatalysts for solar-to-hydrogen peroxide energy conversion. *J. Am. Chem. Soc.* **143**, 12590–12599 (2021).
- Zhang, Y. et al. H₂O₂ generation from O₂ and H₂O on a near-infrared absorbing porphyrin supramolecular photocatalyst. *Nature Energy* **8**, 361–371 (2023).
- Tan, H. et al. Photocatalysis of water into hydrogen peroxide over an atomic Ga-N₅ site. *Nature Synthesis* **2**, 557–563 (2023).
- Zhao, Y. et al. Mechanistic analysis of multiple processes controlling solar-driven H₂O₂ synthesis using engineered polymeric carbon nitride. *Nat. Commun.* **12**, 3701 (2021).
- Zhao, D. et al. Boron-doped nitrogen-deficient carbon nitride-based Z-scheme heterostructures for photocatalytic overall water splitting. *Nat. Energy* **6**, 388–397 (2021).
- Wang, X. et al. A metal-free polymeric photocatalyst for hydrogen production from water under visible light. *Nat. Mater.* **8**, 76–80 (2009).
- Zeng, X. et al. Simultaneously tuning charge separation and oxygen reduction pathway on graphitic carbon nitride by polyethylenimine for boosted photocatalytic hydrogen peroxide production. *ACS Catal.* **10**, 3697–3706 (2020).
- Kofuji, Y. et al. Carbon Nitride-Aromatic Diimide-Graphene Nanohybrids: Metal-Free Photocatalysts for Solar-to-Hydrogen Peroxide Energy Conversion with 0.2% Efficiency. *J. Am. Chem. Soc.* **138**, 10019–10025 (2016).
- Kofuji, Y. et al. Graphitic carbon nitride doped with biphenyl diimide: efficient photocatalyst for hydrogen peroxide production from water and molecular oxygen by sunlight. *ACS Catal.* **6**, 7021–7029 (2016).
- Cheng, H. et al. Rational design of covalent heptazine frameworks with spatially separated redox centers for high-efficiency photocatalytic hydrogen peroxide production. *Adv. Mater.* **34**, e2107480 (2022).
- Wagner, A., Sahm, C. D., Reisner, E. Towards molecular understanding of local chemical environment effects in electro- and photocatalytic CO₂ reduction. **3**, 775–786 (2020).
- Wang, Y. et al. Current understanding and challenges of solar-driven hydrogen generation using polymeric photocatalysts. *Nat. Energy* **4**, 746–760 (2019).
- Luo, J. et al. Photoredox-promoted co-production of dihydroisquinoline and H₂O₂ over defective Zn₃In₂S₆. *Adv. Mater.* **35**, e2210110 (2023).
- Wei, Z. et al. Efficient visible-light-driven selective oxygen reduction to hydrogen peroxide by oxygen-enriched graphitic carbon nitride polymers. *Energy Environ. Sci.* **11**, 2581–2589 (2018).
- Zhang, P. et al. Heteroatom dopants promote two-electron O₂ reduction for photocatalytic production of H₂O₂ on polymeric carbon nitride. **132**, 16343–16351 (2020).
- Zhao, C. et al. Molecular level modulation of anthraquinone-containing resorcinol-formaldehyde resin photocatalysts for H₂O₂ production with exceeding 1.2% efficiency. *Angew. Chem. Int. Ed. Engl.* **62**, e202218318 (2022).
- Ma, P. et al. Band alignment of homojunction by anchoring CN quantum dots on g-C₃N₄ (0D/2D) enhance photocatalytic hydrogen peroxide evolution. *Appl. Catal. B: Environ.* **300**, 120736 (2022).
- Kou, M. et al. Molecularly engineered covalent organic frameworks for hydrogen peroxide photosynthesis. *Angew. Chem. Int. Ed.* **61**, e202200413 (2022).
- Liu, L. et al. Linear conjugated polymers for solar-driven hydrogen peroxide production: the importance of catalyst stability. *J. Am. Chem. Soc.* **143**, 19287–19293 (2021).
- Zhi, Q. et al. Piperazine-linked metalphthalocyanine frameworks for highly efficient visible-light-driven H₂O₂ photosynthesis. *J. Am. Chem. Soc.* **144**, 21328–21336 (2022).
- Zhao, W. et al. Accelerated synthesis and discovery of covalent organic framework photocatalysts for hydrogen peroxide production. *J. Am. Chem. Soc.* **144**, 9902–9909 (2022).
- Fei, H. et al. General synthesis and definitive structural identification of MN₄C₄ single-atom catalysts with tunable electrocatalytic activities. *Nat. Catal.* **1**, 63–72 (2018).
- Cao, L. et al. Identification of single-atom active sites in carbon-based cobalt catalysts during electrocatalytic hydrogen evolution. *Nat. Catal.* **2**, 134–141 (2018).
- Ji, S. et al. Matching the kinetics of natural enzymes with a single-atom iron nanozyme. *Nat. Catal.* **4**, 407–417 (2021).
- Hai, X. et al. Scalable two-step annealing method for preparing ultra-high-density single-atom catalyst libraries. *Nat. Nanotechnol.* **17**, 174–181 (2022).
- Wu, Z.-Y. et al. A general synthesis of single atom catalysts with controllable atomic and mesoporous structures. *Nat. Synth.* **1**, 658–667 (2022).
- Song, S. et al. A selective Au-ZnO/TiO₂ hybrid photocatalyst for oxidative coupling of methane to ethane with dioxygen. **4**, 1032–1042 (2021).
- Chen, R. et al. Charge separation via asymmetric illumination in photocatalytic Cu₂O particles. **3**, 655–663 (2018).
- Wang, G. et al. Synergistic modulation of the separation of photo-generated carriers via engineering of dual atomic sites for promoting photocatalytic performance. *Adv. Mater.* **33**, e2105904 (2021).
- Xiao, X. et al. A promoted charge separation/transfer system from Cu single atoms and C₃N₄ layers for efficient photocatalysis. *Adv. Mater.* **32**, e2003082 (2020).
- Nakamura, R. & Nakato, Y. Primary intermediates of oxygen photo-evolution reaction on TiO₂ (rutile) particles, revealed by in situ FTIR absorption and photoluminescence measurements. **126**, 1290–1298 (2004).
- Jones R. D., Summerville D. A., Basolo F. Synthetic oxygen carriers related to biological systems. **79**, 139–179 (1979).
- Xiao, J. et al. Fast electron transfer and •OH formation: key features for high activity in visible-light-driven ozonation with C₃N₄ catalysts. *ACS Catal.* **7**, 6198–6206 (2017).
- Cao, Y. et al. Hydrogen peroxide electrochemical synthesis on hybrid double-atom (Pd-Cu) doped N vacancy g-C₃N₄: a novel design strategy for electrocatalyst screening. *J. Mater. Chem. A* **8**, 2672–2683 (2020).

49. Guo, X. et al. Simultaneously achieving high activity and selectivity toward two-electron O₂ electroreduction: the power of single-atom catalysts. *ACS Catal.* **9**, 11042–11054 (2019).
50. Kulkarni, A., Siahrostami, S., Patel, A., Nørskov, J.K. Understanding catalytic activity trends in the oxygen reduction reaction. **118**, 2302–2312 (2018).
51. Chen, S. et al. Identification of the highly active Co-N₄ coordination motif for selective oxygen reduction to hydrogen peroxide. *J. Am. Chem. Soc.* **144**, 14505–14516 (2022).
52. Siahrostami, S. et al. Enabling direct H₂O₂ production through rational electrocatalyst design. *Nat. Mater.* **12**, 1137–1143 (2013).
53. Kresse, G. & Furthmüller, J. Efficient iterative schemes for ab initio total-energy calculations using a plane-wave basis set. **54**, 11169 (1996).
54. Perdew, J. P., Burke, K. & Ernzerhof, M. Generalized gradient approximation made simple. *Phys. Rev. Lett.* **77**, 3865–3868 (1996).
55. Blöchl, P. E. Projector augmented-wave method. **50**, 17953 (1994).
56. Grimme, S., Antony, J., Ehrlich, S., Krieg, H. A consistent and accurate ab initio parametrization of density functional dispersion correction (DFT-D) for the 94 elements H–Pu. **132**, 154104 (2010).

Acknowledgements

This work was supported by the National Key Projects for Fundamental Research and Development of China (2021YFA1500803, T.Z.), National Natural Science Foundation of China (12074015 (K.Z.), 51825205 (T.Z.), 22241202 (Q.L.)), the Beijing Outstanding Young Scientists Projects (BJJWZYJH01201910005018, K.Z.), the CAS Project for Young Scientists in Basic Research (YSBR-004, T.Z.), and National Youth Fund (22108093, Y.C.).

Author contributions

X.Z. synthesized and characterized the samples, performed experiments and theoretical calculations, and contributed to the concept of this research. X.Z. and H.S. conceptualized the project. H.S., P.C., and Q.L. provided guidance on XAFS testing and analysis. L.G., Y.C., and Y.W. assisted and guided the theoretical calculations. Y.F., R.F., J.H., X.Z., P.M., H.H., and K.W. assisted in characterization of the samples. Y.Z., C.W., Z.T., and Q.Z. provided constructive suggestions. X.Z., H.S., Q.L., T.Z., and K.Z. analysed the experimental results and wrote the

manuscript. K.Z. led the entire project. All authors read the manuscript and contributed to the discussion of the results.

Competing interests

The authors declare no competing interests.

Additional information

Supplementary information The online version contains supplementary material available at <https://doi.org/10.1038/s41467-023-42887-y>.

Correspondence and requests for materials should be addressed to Qinghua Liu, Tierui Zhang or Kun Zheng.

Peer review information *Nature Communications* thanks the anonymous reviewers for their contribution to the peer review of this work. A peer review file is available.

Reprints and permissions information is available at <http://www.nature.com/reprints>

Publisher's note Springer Nature remains neutral with regard to jurisdictional claims in published maps and institutional affiliations.

Open Access This article is licensed under a Creative Commons Attribution 4.0 International License, which permits use, sharing, adaptation, distribution and reproduction in any medium or format, as long as you give appropriate credit to the original author(s) and the source, provide a link to the Creative Commons license, and indicate if changes were made. The images or other third party material in this article are included in the article's Creative Commons license, unless indicated otherwise in a credit line to the material. If material is not included in the article's Creative Commons license and your intended use is not permitted by statutory regulation or exceeds the permitted use, you will need to obtain permission directly from the copyright holder. To view a copy of this license, visit <http://creativecommons.org/licenses/by/4.0/>.

© The Author(s) 2023